International Journal of Aeronautical and Space Sciences (2021) 22:1048–1061
https://doi.org/10.1007/s42405-021-00390-y

IJASS International Journal of Aeronautical and Space Sciences

ORIGINAL PAPER

Cable Suspension and Balance System with Low Support Interference and Vibration for Effective Wind Tunnel Tests

Keum-Yong Park[1,3] · Yeol-Hun Sung[2,3] · Jae-Hung Han[3]

Received: 30 November 2020 / Revised: 5 May 2021 / Accepted: 11 May 2021 / Published online: 14 June 2021
© The Author(s) 2021

Abstract
A cable-driven model support concept is suggested and implemented in this paper. In this case, it is a cable suspension and balance system (CSBS), which has the advantages of low support interference and reduced vibration responses for effective wind tunnel tests. This system is designed for both model motion control and aerodynamic load measurements. In the CSBS, the required position or the attitude of the test model is realized by eight motors, which adjust the length, velocity, and acceleration of the corresponding cables. Aerodynamic load measurements are accomplished by a cable balance consisting of eight load cells connected to the assigned cables. The motion responses and load measurement outputs were in good agreement with the reference data. The effectiveness of the CSBS against aerodynamic interference and vibration is experimentally demonstrated through comparative tests with a rear sting and a crescent sting support (CSS). The advantages of the CSBS are examined through several wind tunnel tests of a NACA0015 airfoil model. The cable support of the CSBS clearly showed less aerodynamic interference than the rear sting with a CSS, judging from the drag coefficient profile. Additionally, the CSBS showed excellent vibration suppression characteristics at all angles of attack.

Keywords Cable suspension and balance system · Support interference · Vibration · Wind tunnel test

1 Introduction

A wind tunnel test, commonly used in experimental fluid dynamics (EFD), is capable of investigating the aerodynamic characteristics of test objects under various test conditions, such as extreme angles of attack and low Reynolds numbers [1, 2]. Various new techniques have been developed and introduced in the wind tunnel testing community, particularly in relation to flow quality control, flow visualization, and improved balance, among others. Occasionally, a water tunnel takes its place for better Reynolds number similarity and improved flow visualization [3–5]. Recently, even an emulated flutter wind tunnel test was proposed [6].

✉ Jae-Hung Han
jaehunghan@kaist.ac.kr

[1] Agency for Defense Development, Yuseong, P.O. Box 35, Daejeon 34186, Republic of Korea

[2] Aeronautics Technology Research Division, Korea Aerospace Research Institute, 169-84 Gwahak-ro, Yuseong-gu, Daejeon 34133, Republic of Korea

[3] Department of Aerospace Engineering, KAIST, 291 Daehak-ro, Yuseong-gu, Daejeon 34141, Republic of Korea

A support structure is an essential device in wind tunnel tests, and this component must hold the test model firmly [7–9] while also accommodating tubes and electrical wires. It should also be capable of motion control in order to change the attitude of the model. Several sting and motion control mechanisms have been applied to test models to meet these requirements. However, these large structures usually occupy much space inside the test section and can often block the flow.

Support interference acts to distort the flow field due to the support structure. It can be interpreted as the aerodynamic interaction between the model and the support structure. Support interference can result in different aerodynamic characteristics between the test article and the actual article. Support systems and support interference are among the main areas of investigation in experiments on aerodynamics, as they can significantly influence the accuracy of test outcomes [10, 11].

The sting vibration is also considered to be an important topic in relation to wind tunnel testing. Long cantilever stings inevitably undergo vibration in the mounted model, and the overload induced by the vibration often results in an unexpected test termination. This problem is

further complicated when the model passes through a stall, resulting in nonlinear lift load changes [12]. Many efforts have been made to suppress sting vibrations by increasing the sting system damping either by passive or active methods[13, 14].

There have been various attempts to avoid the adverse effects of conventional model supports. Data correction procedures are commonly employed to compensate for aerodynamic interference due to model supports [15, 16]. A magnetic suspension and balance system (MSBS) has also been proposed. Using the MSBS, levitation of the test model is possible, removing any mechanical contact by controlling the direction and magnitude of the magnetic fields [17, 18]. However, this approach is considered to be overly complicated and too costly to be utilized for general-purpose testing.

As a new approach, a cable-driven parallel robot (CDPR) induces less aerodynamic interference than conventional model supports. The test area can be extended further than that with the MSBS for general-purpose wind tunnel tests. The CDPR can also maintain appropriate stiffness levels. Recently, various studies have applied CDPRs an attitude control systems in wind tunnel tests [19–27]. The capabilities of a CDPR can be enhanced such that it can function as a load measuring balance by adding appropriate sensors to cables. For instance, it was reported that the Railway Technical Research Institute operated a 6-component cable balance in Leeward wind tunnel [28]. In the cable balance, one end of the steel cable is fixed onto the test model and the other end is connected to a load cell to measure the aerodynamic load. In this case, the cable balance consists of ten load cells. This cable balance is a good example that demonstrates the possibility of a cable mechanism as a load measurement device. It is expected that an appropriate combination of a CDPR and a cable balance can allow the construction of a multi-purpose system that can perform both motion control and load measurements simultaneously in wind tunnel tests.

The main objective of the present study was to introduce an alternative type of model support capable of reducing the aerodynamic interference and vibration of the conventional model support. As a possible candidate, a cable model support mechanism is suggested. The suggested mechanism is based on the cable-driven parallel robot (CDPR) formulation. Additionally, the motion control capabilities of the CDPR are augmented by a load measurement function. We refer to this system as a cable suspension and balance system (CSBS) in accordance with the acronym MSBS at KAIST, emphasizing its role as a balance. It is expected that this system will effectively overcome the disadvantages of sting or strut supports. The CSBS was designed to realize accurate roll, pitch, and yaw motions and to allow easy configuration changes of the test model for general-purpose wind tunnel tests. The CSBS was implemented with ball screw base linear actuators for accurate motion and eight load cells for precise aerodynamic load measurements.

The performance of the CSBS prototype was verified through several motion tests and load measurements. A motion tracking system measured the motion responses, with the loading outputs from the precise six-component balance used here. The test results showed good agreement with the reference data, implying that the developed CSBS is a reliable multi-purpose device capable of simultaneously performing accurate motion control and load measurements.

The effectiveness of the CSBS against aerodynamic interference and vibration was experimentally demonstrated through comparative tests with a conventional sting support. A modified NACA0015 airfoil model was chosen for the wind tunnel tests. In this study, the typical configuration of a crescent sting support (CSS) with a rear sting was employed for comparison with the newly developed cable support configuration of the CSBS. The cable support of the CSBS clearly showed much less aerodynamic interference compared to that when using the rear sting with a CSS, judging from the drag coefficient profile of the tests. In addition, the CSBS showed excellent vibration attenuation characteristics at all AOA settings, even in a stall range that a conventional cantilever sting frequently could not reach due to severe vibration. These characteristics could allow us easily to expand the test envelope of a wind tunnel.

2 Background Theory and Formulation

2.1 Cable Length from Inverse Geometry

The cable suspension and balance system (CSBS) can control the experimental model's position/attitude and measure the aerodynamic load via several cables in wind tunnel tests. In the CSBS, the final position and attitude of the test model are determined by the lengths of the eight cables used. Each cable length can be derived from the inverse geometry of the CSBS, as described in Fig. 1. The cable vector, $\boldsymbol{l}_i^b$ is defined by relevant position vector, as follows [29]. Eventually, the magnitude of vector $\boldsymbol{l}_i^b$ becomes the cable length l_i.

$$\boldsymbol{l}_i^b = \boldsymbol{a}_i^b - \boldsymbol{t} - \mathbf{R}\boldsymbol{b}_i^p, \quad i = 1, \ldots, 8. \tag{1}$$

Here, $\boldsymbol{a}_i^b$ indicates the position vector of A_i and $\boldsymbol{t} = \left[t_X, t_Y, t_Z\right]^T$ is the position vector of origin O_p. $\boldsymbol{b}_i^p$ is the vector pointing from origin O_p to attachment point B_i in moving frame F_p. $\mathbf{R}$ is the rotation matrix defining the test model orientation. It contains the roll, pitch, and yaw angles (ϕ, θ, and ψ) with respect to the X_b, Y_b, and Z_b axes, respectively, and is defined as follows [29]:

$$\mathbf{R} = \mathbf{R}_Z(\psi)\mathbf{R}_Y(\theta)\mathbf{R}_X(\phi), \tag{2}$$

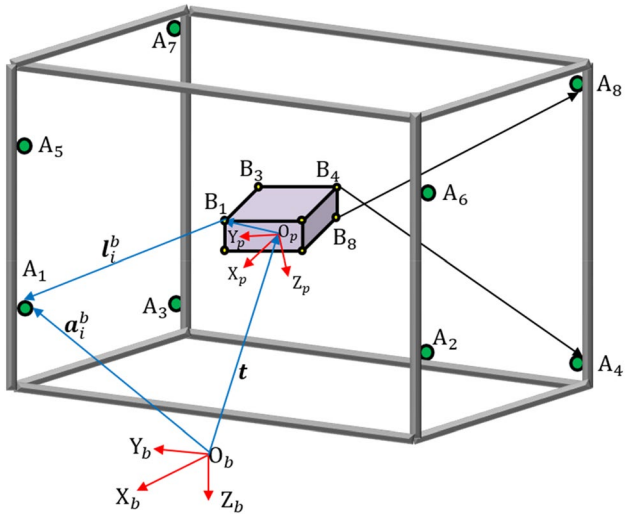

Fig. 1 General schematic of the CSBS

where

$$\mathbf{R}_X(\phi) = \begin{bmatrix} 1 & 0 & 0 \\ 0 & \cos\phi & -\sin\phi \\ 0 & \sin\phi & \cos\phi \end{bmatrix}, \quad \mathbf{R}_Y(\theta) = \begin{bmatrix} \cos\theta & 0 & \sin\theta \\ 0 & 1 & 0 \\ -\sin\theta & 0 & \cos\theta \end{bmatrix},$$

$$\mathbf{R}_Z(\varphi) = \begin{bmatrix} \cos\psi & -\sin\psi & 0 \\ \sin\psi & \cos\psi & 0 \\ 0 & 0 & 1 \end{bmatrix}.$$

2.2 Pulley Geometry Correction

In a simplified model of the CSBS, the *i*th pulley exit point A_i is considered as a fixed point. However, during actual motion, the pulley exit point moves along the circumference of the pulley following the test model motion, as described in Fig. 2. As a result, the coordinate of A_i should be replaced with A_i', which varies according to the model pose $\mathrm{p} = \left[t^T, r^T\right]^T$. The corrected value of A_i' depends on the pulley radius and on the magnitude of motion. Each pulley has two rotating axes which allow the test model to move in 3D space upon changes of the cable length and direction.

In Fig. 3, the pulley plane of the i-th cable is described as local frame F_i with origin A_i and axes $\boldsymbol{x}_i$, $\boldsymbol{y}_i$ and $\boldsymbol{z}_i$. Axes $\boldsymbol{x}_i$ and $\boldsymbol{y}_i$ construct the pulley plane and axis $\boldsymbol{x}_i$ lies along the direction of the corresponding actuator. Axis z_i lies perpendicular to both axes, and i indicates the pulley number ($i = 1, \ldots, 8$). The pulley plane has a tilting angle about axis $\boldsymbol{x}_i$; this can be derived from the following equation [29]:

$$\tan\left(\phi_i\right) = \frac{l_{z,i}}{l_{y,i}}, \tag{3}$$

where $l_{y,i}$ and $l_{z,i}$ are the y and z-components of $\boldsymbol{l}_i^b$ in the fixed reference frame F_b, respectively. After finding the tilting angle, the position vector of the pulley center O_i is computed as follows [29]:

$$\boldsymbol{o}_i^b = \boldsymbol{a}_i^b + r_p \boldsymbol{R}_i \boldsymbol{y}_i = \boldsymbol{a}_i^b + r_p \boldsymbol{y}_i^b, \tag{4}$$

where r_p represents the radius of the pulley and $\boldsymbol{R}_i$ is the rotation matrix of tilting angle ϕ_i. The components of $\boldsymbol{R}_i$ can be written as follows [29]:

$$\boldsymbol{R}_i = \begin{bmatrix} 1 & 0 & 0 \\ 0 & \cos\phi_i & -\sin\phi_i \\ 0 & \sin\phi_i & \cos\phi_i \end{bmatrix}. \tag{5}$$

If a $\boldsymbol{h}_i$ is defined as the unit direction vector from the pulley center point O_i to the pulley exit point A_i' in frame F_i, it can be derived from the cable wrap angle $\alpha_i = \alpha_{i,1} + \alpha_{i,2}$, the components of which are as follows [29]:

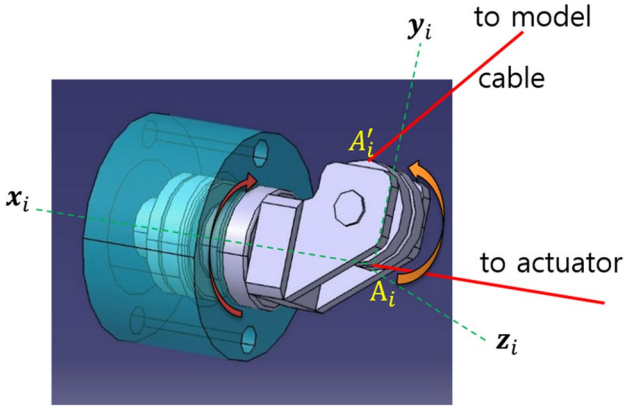

Fig. 2. 3D CAD model of a pulley with two axes of rotation

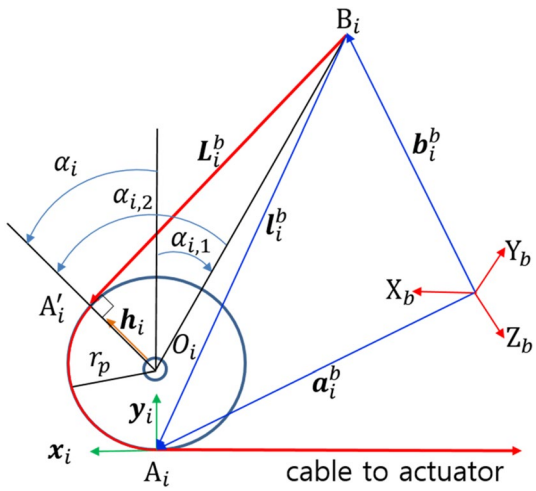

Fig. 3. 2D schematic of pulley correction

$$\sin\alpha_{i,1} = \frac{\left(\boldsymbol{b}_i^b - \boldsymbol{o}_i^b\right)^T \boldsymbol{x}_i^b}{\left\|\boldsymbol{b}_i^b - \boldsymbol{o}_i^b\right\|_2}, \tag{6}$$

$$\sin\alpha_{i,2} = \frac{r_p}{\left\|\boldsymbol{b}_i^b - \boldsymbol{o}_i^b\right\|_2}. \tag{7}$$

The corrected cable vector $\boldsymbol{L}_i^b$ extends from the model attachment point B_i to the actual pulley exit point $A_i^{'}$, and it can be described in the fixed reference frame F_b as follows [29]:

$$\boldsymbol{L}_i^b = \boldsymbol{a}_i^b + r_p\left(\boldsymbol{R}_i\boldsymbol{y}_i + \boldsymbol{R}_i\boldsymbol{h}_i\right) - \boldsymbol{b}_i^b. \tag{8}$$

Consequently, the magnitude of $\boldsymbol{L}_i^b$ leads to the corrected cable length, L_i.

2.3 Cable Speed from Inverse Kinematics

For motion control of the CSBS, the speed of each cable is a significant factor to be considered, in addition to the cable length. Appropriate speed control of the cable is essential to enable its role as a support structure and actuator. If each cable is not at the proper speed, some cables may have more or less tension than required, which eventually leads to a loss of its function as a structure or can even lead to cable breakage. The speed of each cable can be derived from the inverse kinematics of the CSBS [29, 30]. If the velocity/angular velocity of the model and the Jacobian of the CSBS are given, the speed assigned to each cable can be estimated as follows:

$$\dot{L} = J\dot{Q}, \tag{9}$$

where $\dot{L} = [\dot{L}_1, \dot{L}_2, \ldots, \dot{L}_m]^T$ is the cable velocity vector and $\dot{Q} = \left[\dot{X}, \dot{Y}, \dot{Z}, \dot{\phi}, \dot{\theta}, \dot{\psi}\right]^T$ is the linear/angular velocity vector of the test model. The notation $\mathbf{J}$ represents the inverse kinematic Jacobian matrix for the CSBS and is composed of the first derivatives of a cable length with respect to the 6-DOF variable, as described in Eq. (10).

$$\mathbf{J} = \begin{bmatrix} \frac{\partial L_1}{\partial X} & \frac{\partial L_1}{\partial Y} & \frac{\partial L_1}{\partial Z} & \frac{\partial L_1}{\partial \phi} & \frac{\partial L_1}{\partial \theta} & \frac{\partial L_1}{\partial \psi} \\ \frac{\partial L_2}{\partial X} & & \ddots & & & \vdots \\ \vdots & & \cdots & & & \vdots \\ & \frac{\partial L_m}{\partial X} & \cdots & \frac{\partial L_m}{\partial \psi} & & \end{bmatrix}. \tag{10}$$

2.4 Load Measurement from Cable Tension

The function of a CSBS can be extended to include load measurements through the appropriate deployment of force sensors. In the equilibrium condition, the tension forces of the eight cables must be balanced with the external load exerted on the test model. This external load can be represented as a six-dimensional vector expressed in frame F_b, as follows [31]:

$$\boldsymbol{w}_e = \left[\boldsymbol{f}_e^T, \boldsymbol{m}_e^T\right]^T = \left[f_x, f_y, f_z, m_x, m_y, m_z\right]^T, \tag{11}$$

where f_x,f_y,f_z, m_x, m_y and m_z are the x, y and z components of the external force and moment vectors, respectively. The tension $\boldsymbol{\tau}$ in the eight cables is balanced with the external load $\boldsymbol{w}_e$, according to the equation below.

$$\mathbf{W}\boldsymbol{\tau} + \boldsymbol{w}_e = 0. \tag{12}$$

The cable tension values are collected in tension vector $\boldsymbol{\tau} = \left[\tau_1, \tau_2, \ldots, \tau_m\right]^T$ and are multiplied by matrix $\mathbf{W}$ (the wrench matrix in the robotics community) to be transformed to a six-component load. Matrix $\mathbf{W}$ is defined as shown below.

$$\mathbf{W} = \begin{bmatrix} \boldsymbol{d}_1^b & \boldsymbol{d}_2^b & \cdots & \boldsymbol{d}_m^b \\ \boldsymbol{R}\boldsymbol{b}_1^p \times \boldsymbol{d}_1^b & \boldsymbol{R}\boldsymbol{b}_2^p \times \boldsymbol{d}_2^b & \cdots & \boldsymbol{R}\boldsymbol{b}_m^p \times \boldsymbol{d}_m^b \end{bmatrix}. \tag{13}$$

The relationship between wrench matrix $\mathbf{W}$ and the inverse kinematic Jacobian matrix $\mathbf{J}$ is described in Eq. (14), and this can be derived from the virtual work principle [30]. The inverse kinematic Jacobian matrix $\mathbf{J}$ is eventually applied to the calculation of the cable velocity in Eq. (9).

$$\mathbf{J} = -\boldsymbol{W}^T. \tag{14}$$

The aerodynamic load can be acquired by force sensors, which are connected to the cable in the CSBS, by measuring the change in the tension during the wind tunnel test. Load measurement capabilities were added to the CSBS by adding eight load cells to the corresponding cables routed to the test model via pulleys. Each pulley was needed to be positioned to keep the cable direction perpendicular to the assigned load cell and was designed to maintain low friction. These arrangements allow the load cells to measure the cable tension more accurately. Figure 4 shows a schematic of the load measurement process used by the CSBS.

3 Hardware and Software of the CSBS

3.1 Sub-systems and Integration

The development of the CSBS was accomplished through careful design, fabrication, and integration processes. It requires mechanical/electrical hardware and integrated software. The CSBS consists of six sub-systems: a mainframe for the cable suspension device, a motion control system, a motion tracking system that acquires the 6-DOF motion data, a load measurement system, integrated control software, and a test model [32]. The CSBS mainframe consisted of commercial aluminum profiles to support all

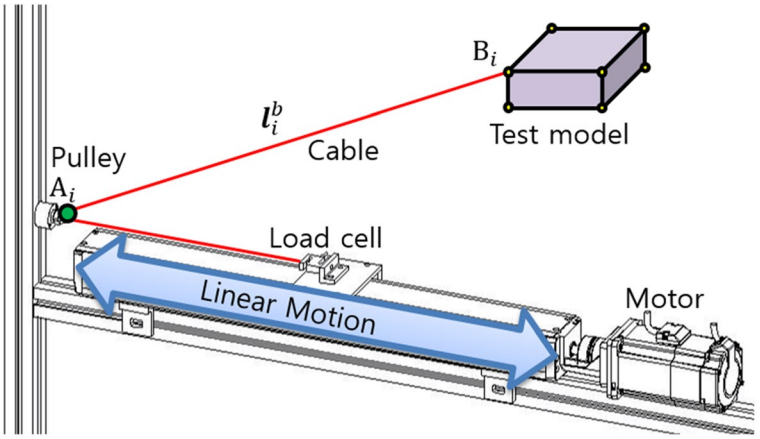

Fig. 4 Load measurement schematic

actuating and suspension parts. The size of the mainframe is 1200 × 1500 × 1300 mm in the *X*, *Y*, and *Z* directions, respectively, in the fixed reference frame F_b. In the motion control system, eight motor drivers generate feedback control signals for the servo motors according to the cable length and velocity commands using a proportional–integral–differential (PID) control module. For accurate motion control, ball screw linear modules with a 500 mm stroke were utilized.

A motion tracking system was installed to monitor the 6-DOF movement trajectory of the test model. It consists of four IR cameras with a 1664 × 1088 resolution and an associated control system. It is a vision-based positioning system capable of acquiring real-time high-precision position data from the test model over a wide range without mechanical contact [17]. The motion tracking system can acquire 6-DOF position and attitude data at 360 frames per second (FPS). The accuracy of the system is defined in terms of the root mean square error (RMSE), and it appears to be less than 0.05 mm, which is the camera calibration result from the dedicated software used in the system.

The load measurement system includes a cable balance consisting of eight load cells and data acquisition (DAQ) devices. Load cells with a capacity of 300 N and steel cable with a diameter of 0.85 mm were chosen for the cable balance. This load cell and steel cable combination was based on a fail-safe concept. In case of an overload, the selected steel cable is designed to break before the load cell is damaged. The cable for the CSBS should have enough strength to act as a supporting structure and maintain flexibility simultaneously to be bent according to the pulley's circumference. Also, considerable elongation should be avoided when selecting the CSBS cable because this can have undesirable effects on both motion control and the load measurement performance. A strength test was carried out for candidate cables, polyethylene, and steel cable, to find most suitable the cable for the CSBS that meets all of its requirements. Figure 5 shows the result of this test, in the form of a tension vs. elongation plot. The results indicate that the steel cable is much more appropriate for the CSBS. In the test results, the failure strength of the steel cable is approximately 24 kgf. This provides a guideline for the fail-safe selection of a load cell Fig. 6.

The integrated control software was designed to supply motion commands, display the measured data, and save the selected data. It calculates the cable length and speed

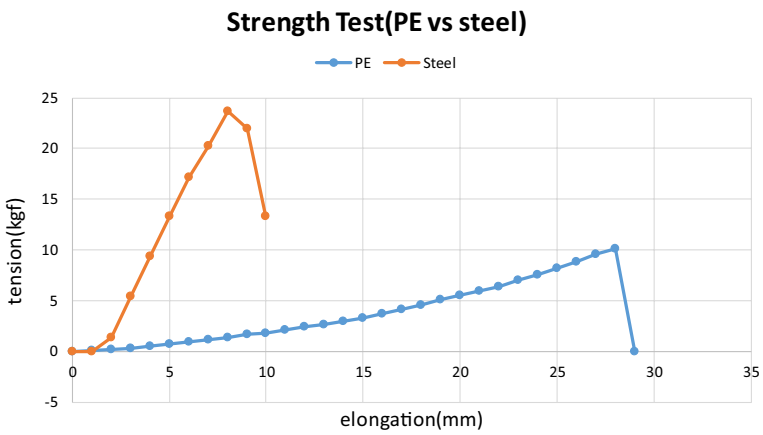

Fig. 5 Strength test of the candidate cables

for the assigned motion command based on the CSBS formulations presented in the previous section. It also transforms the data from the eight load cells into three forces and three moments. All of the command and measurement data run through a serial connection or Ethernet line. The integrated control software acts as a translator between the user and the hardware.

The test model was designed to allow easy cable connections. Several infrared reflectors were attached to the model surface for 6-DOF pose detection by the motion tracking system. A NACA0015 airfoil model (Chord: 200 mm, Span: 400 mm) was prepared for the wind tunnel test.

The primary electric devices for the CSBS are assembled into the rack frame. Figure 7 shows a 19-inch rack system used here, integrating the electric hardware of the CSBS, including an emergency stop device and a power supply. The green box indicates the eight motor drivers, the red box is the NI cDAQ device, and the blue box shows the Ethernet connection hub for the cameras.

Figure 8 shows the overall configuration of the mechanical hardware for the CSBS. The motion control command is applied to the motor drivers via the integrated control software. The motor control signals of the drivers arrive at the assigned servo motors to activate the connected linear actuators. The measured signals from the IR cameras are collected by the motion tracking system and converted to 6-DOF data by the dedicated software. The low-level electric signals from the eight load cells are amplified through the load measurement system. The measured data are displayed in various plots and indicators on the user interface screen.

Fig. 7 19-inch rack system integrating the electric hardware

3.2 Performance of the CSBS

Several motion tests were carried out on the CSBS prototype to investigate its motion control performance. In this test, a single DOF motion command was applied sequentially from the *X*-direction to the RZ-direction. The test range and intervals are listed in Table 1, where *X*, *Y*, and *Z* are the translational DOFs, and RX, RY, and RZ are the rotational DOFs in the fixed reference frame. During the single DOF motion, the other five DOF motion commands were set to a position or angle of zero.

The CSBS prototype exhibited fairly good motion control performance. The motion responses showed good agreement

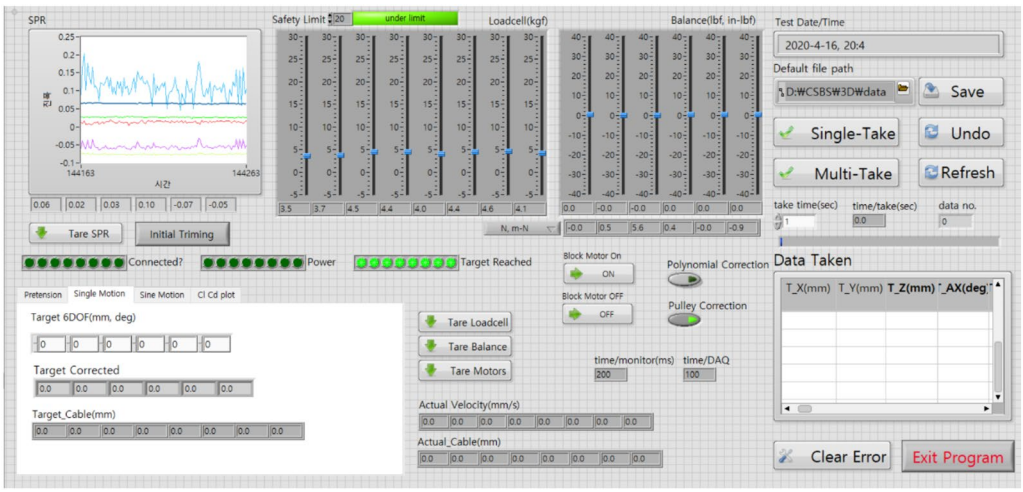

Fig. 6 CSBS integrated control software

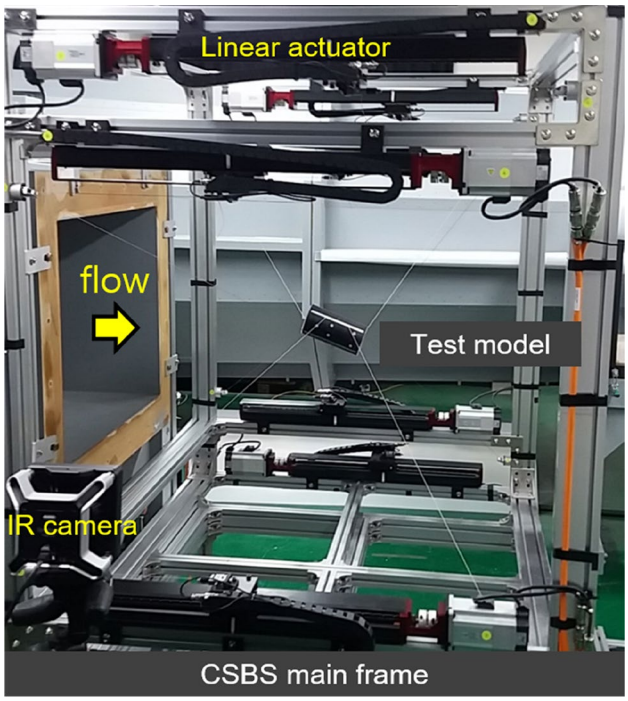

Fig. 8 Mechanical hardware for the CSBS [32]

with the motion commands for all directions. The last row in Table 1 presents the motion control accuracy of the CSBS using the root mean square errors (RMSE). This statistical data confirm that the developed CSBS has accurate and precise motion control capabilities [32].

The CSBS was designed to act as a balance for aerodynamic load measurements and as a motion control device in wind tunnel tests. Several loading tests were carried out on the CSBS prototype to investigate the load measurement performance, including its accuracy [32].

A load adaptor, reference balance, and a test model were connected mechanically in series. Then, eight cables were routed from the test model to the assigned load cells via pulleys. This mechanism made it possible to compare the load from the reference balance with that from the cable balance. When any test load from outside acted on the loading adaptor, it was measured by the six component balance in the form of three forces and three moments and was simultaneously transmitted to the eight load cells, which were mechanically connected through cables [32].

During the loading tests, arbitrary loads were applied to the loading adaptor for 40 s, with various positions and attitudes, to acquire unsteady load data. The detailed loading sequence was presented in our previous paper, reference [32]. To observe the load measurement performance clearly and quantitatively, several statistical analyses were carried out with the loading test data. In these analyses, a precise balance was applied as a reference sensor to be compared. Table 2 summarizes the maximum loading and the analysis results. The load measurement accuracy of the CSBS was presented using the root means square error values (RMSE). The RMSE values appeared to be very small for all six components, as shown in Table 2. Through these analyses, it was confirmed that the CSBS could accurately measure aerodynamic loads.

4 Verification of the CSBS in Wind Tunnel Tests

4.1 Preparation for the Comparative Tests

CSBS application experiments were conducted to investigate the reliability of the CSBS as a model support and load measurement system at a low-speed wind tunnel located at the Agency for Defense Development (ADD) in Korea. The size of the cross-section is 750 × 560 mm. Ahead of the test section, a honeycomb, screens, and a cooling system were installed in the contraction section. These systems allow a more uniform, low-turbulence flow for wind tunnel tests. The contraction ratio is 9.0, and the wind speed is controllable from 10 to 100 m/s. The crescent sting support (CSS) used in the tests is a motor-driven device that can convert

Table 1 Motion test conditions and motion control accuracy [32]

Direction	Translation			Rotation		
	X (mm)	*Y* (mm)	*Z* (mm)	RX (deg)	RY (deg)	RZ (deg)
Test range	±200	±200	±160	±30	±30	±16
Test interval	10.0	10.0	10.0	1.0	1.0	1.0
RMSE	0.06	0.05	0.15	0.21	0.04	0.09

Table 2 Maximum loading and measurement accuracy [32]

Component	FX (*N*)	FY (*N*)	FZ (*N*)	MX (*N*-m)	MY (*N*-m)	MZ (*N*-m)
Max. loading	109	75	104	4	6	3
RMSE	0.98	1.34	0.91	0.06	0.07	0.04

linear motion to angular motion, controlling the required AOA very accurately with a ball screw mechanism. This type of AOA control device has been widely adopted in wind tunnels. The ADD also operates a CSS and frequently applies it in various tests. In this study, the conventional configuration of a rear sting and the CSS was employed for comparison with the newly developed cable support configuration of the CSBS. Between a test model and rear sting, a precise six-component balance is installed. The balance selected for the test has a 12 mm diameter and length of 100 mm. Its repeatability error is less than 0.15% of the maximum loading capacity. This balance was utilized as a reference loading sensor and was applied to the comparative wind tunnel test with the rear sting support.

The NACA0015 airfoil model was chosen for use in the comparative wind tunnel tests. This model was applied to investigate the model support interference and vibration. Distortion of the airfoil shape is inevitable when installing the NACA0015 airfoil model on an internal balance with a rear sting. The center part of the airfoil model was modified to allow space for the balance, balance adaptor, and rear sting installation path.

Several reflectors were attached to the left side of the airfoil as the target objects of the motion tracking system, providing the pitch angle of the NACA0015during the wind tunnel tests. The position of the zero pitch angle was achieved using laser level system, providing the alignment line between the airfoil and the flow center of wind tunnel as described in Fig. 9. The flow angularity was examined through the C_L vs AOA plots. Because the shape of the NCA0015 is symmetrical, the AOA that C_L curve crosses zero indicates the flow angularity of the wind tunnel. This value was applied to AOA data correction.

A set of particular clamping apparatuses was devised to fix the airfoil model into an initial position/attitude and to apply pretension for the CSBS. Figure 9 shows that the clamping apparatus was removed from the airfoil model after the pretension process.

Initially, two model support configurations were prepared to acquire the aerodynamic data from the modified airfoil model. The first utilized a rear sting support with the CSS, as shown in Fig. 10, and the second used a cable support with the CSBS, as shown in Fig. 11. However, another test configuration was required to estimate the support interference effect due to the rear sting and cable support. The third configuration is shown in Fig. 12. This configuration consists of the cable support, a dummy sting, and the CSS. The shape of the dummy sting is identical to that of the rear sting mentioned earlier. It is assumed to have the same aerodynamic interference as an actual rear sting. However, the dummy sting has no mechanical contact with the test model. In this configuration, the aerodynamic load is measured by the cable balance of the CSBS.

Comparing the configuration depicted in Fig. 10 with that in Fig. 12, the only difference between the two figures is the existence of cables. It can be expected that the support interference due to the cable of the CSBS can be estimated according to the differences in the aerodynamic data from the wind tunnel tests of the two configurations. Similarly,

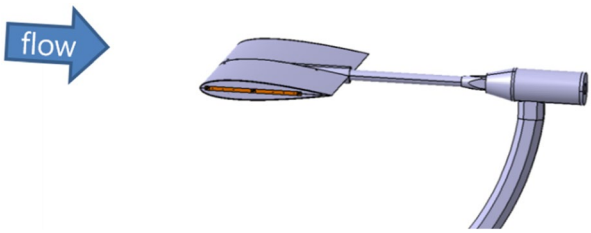

Fig. 10 Rear sting support with the CSS

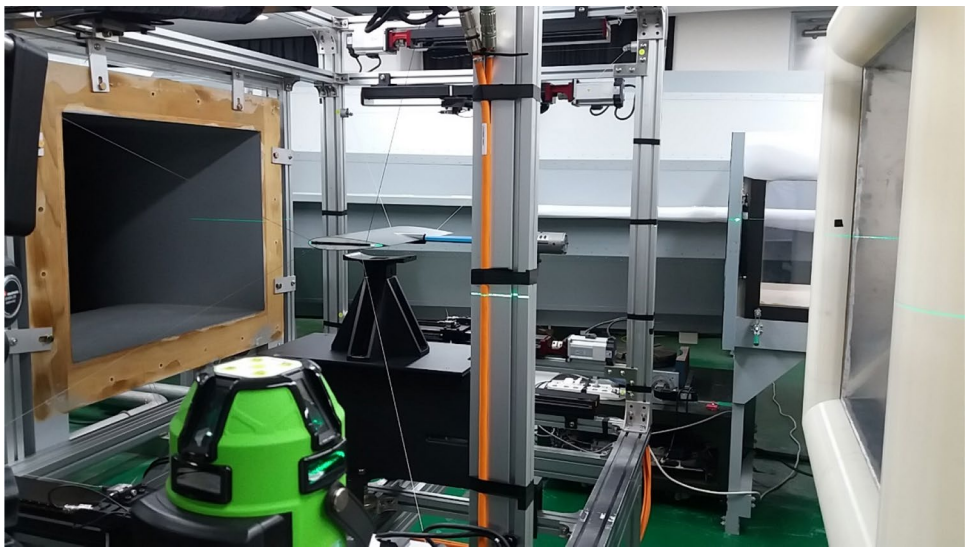

Fig. 9 Zero positioning with a laser level system

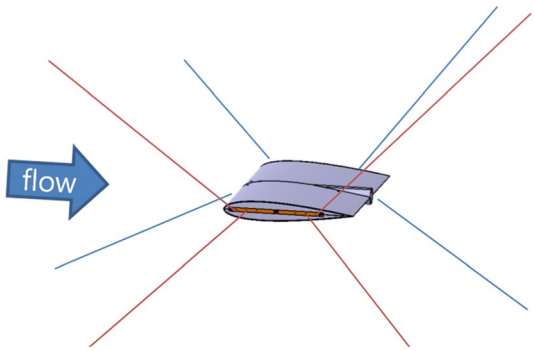

Fig. 11 Cable support of the CSBS

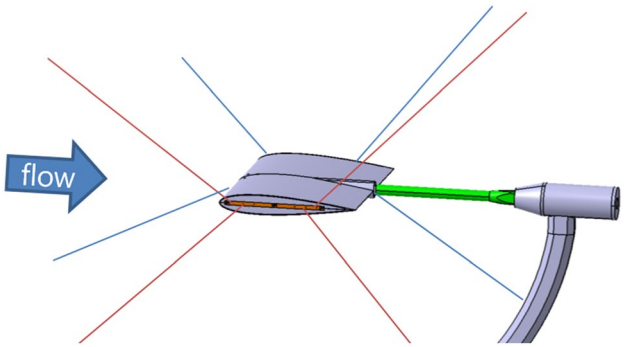

Fig. 12 Cable support and the dummy sting with the CSS

comparing the configuration depicted in Fig. 11 with that in Fig. 12, the only difference between the two figures is the rear sting support with the CSS. The support interference due to the rear sting with the CSS can also be estimated by considering the differences in the aerodynamic data for these two configurations.

4.2 Model Support Interference

Various wind tunnel tests were conducted using the three configurations explained in the previous section to investigate experimentally the support interference due to the rear sting support and the cable support of the CSBS. For the first test configuration, the aerodynamic data were acquired, which included the interference effect due to the rear sting support shown in Fig. 13. In this configuration, the modified NACA0015 airfoil was supported by the rear sting, and the AOA was controlled by the CSS. A weight tare test with an AOA-sweep process was conducted without wind. The tare data are subtracted from measured load during wind-on tests to remove the effect due to gravity.

The lift and drag coefficients were acquired for three Reynolds number cases (440,000, 500,000, 550,000). The angle of attack (AOA) of the airfoil was varied from − 4°–25° at 1° intervals using the CSS. Six component aerodynamic loads were measured by a precision internal balance in three forces and three moments. All measured data were saved at 10 Hz every 5 seconds in each assigned AOA and the data were averaged during a post process.

In the second test configuration of Fig. 14, the modified NACA0015 airfoil was suspended by eight cables. Wind tunnel tests were conducted to acquire the aerodynamic data, which included the interference effect due to the cable support. As before, a tension tare test with AOA-sweep was conducted without wind. The tare data were subtracted from the acquired load to remove the effects of gravity and the initial tension for each AOA.

The lift and drag coefficients were acquired in conditions identical to those in the previous rear sting configuration, including the Reynold numbers and AOA values. However, the angle of attack (AOA) of the test model was controlled

Fig. 13 Wind tunnel test with the rear sting support and CSS

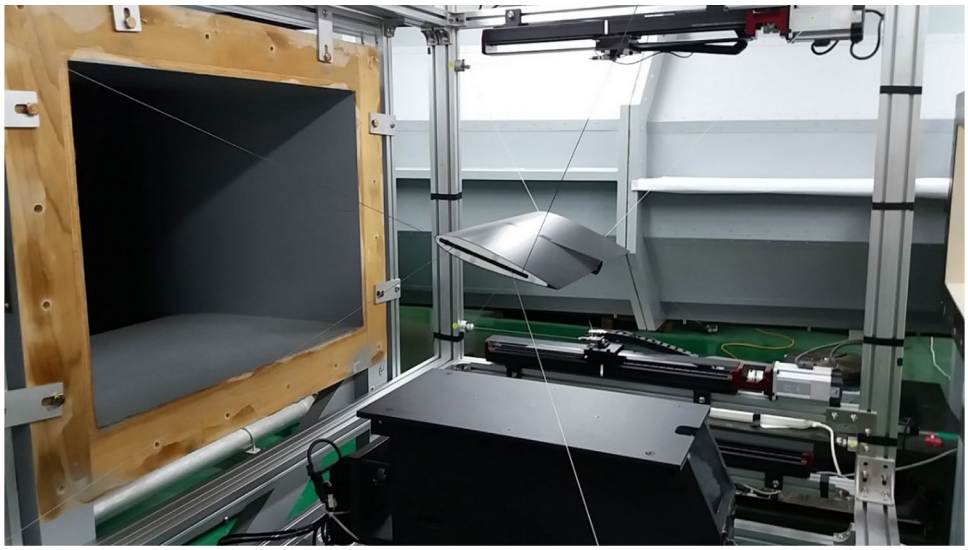

Fig. 14 Wind tunnel test with the cable support of the CSBS

by the CSBS. The outputs from the eight load cells were converted and corrected to three forces and three moments.

For the third test configuration in Fig. 15, wind tunnel tests were carried out to collect the aerodynamic data, which included the interference effect due to both the rear sting support and the cable support in this case. For the tare test, the same procedures of the cable support configuration were repeated.

The lift and drag coefficients were acquired from identical conditions, i.e., from Reynolds numbers and AOA values identical to those in the two previous configurations. In these tests, motion control of the test model and the aerodynamic load measurement were conducted by the CSBS. However, the dummy sting motion was controlled by the CSS following the AOA of the test model independently. The dummy sting was mechanically separated from the airfoil model. There was no load path between the airfoil model and the dummy sting, except for the aerodynamic interference.

Figures 16, 17, and 18 summarize the test results from the three aforementioned configurations for each Reynolds number of 440,000, 5,000,000, and 550,000. These figures present comparative profiles for the lift and drag coefficients among the three configurations when increasing the model AOA. JavaFoil program results are also added as reference aerodynamic coefficient data for comparison.

In the C_L plots of Fig. 16, it is not easy to find differences among the test results for the three configurations. The C_L test results with the increased Reynolds numbers are presented in Figs. 17 and 18. These two figures show identical characteristics, indicating that the interference effects due to the model supports applied here are not very significant with regard to the lift coefficient. The three C_L plots clearly show

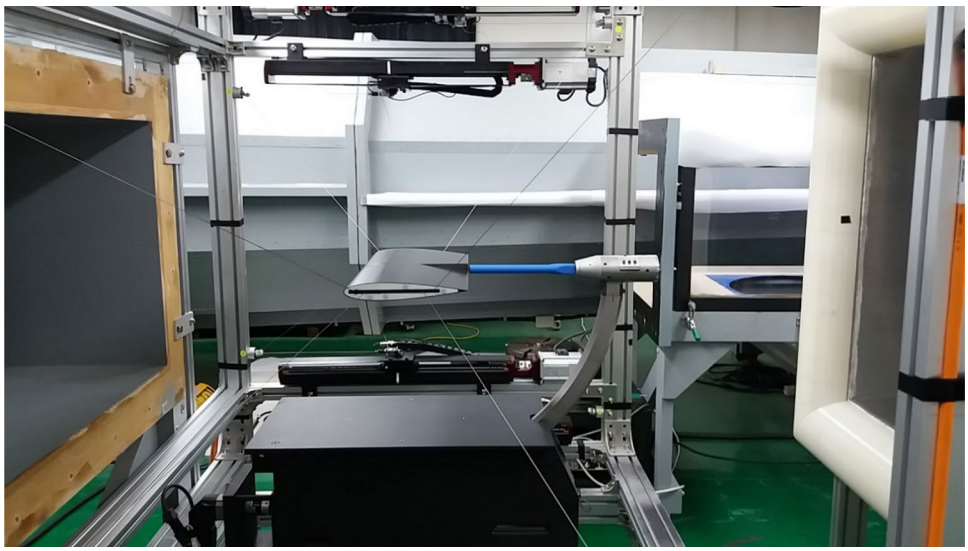

Fig. 15 Wind tunnel test with the cable support, the dummy sting and the CSS

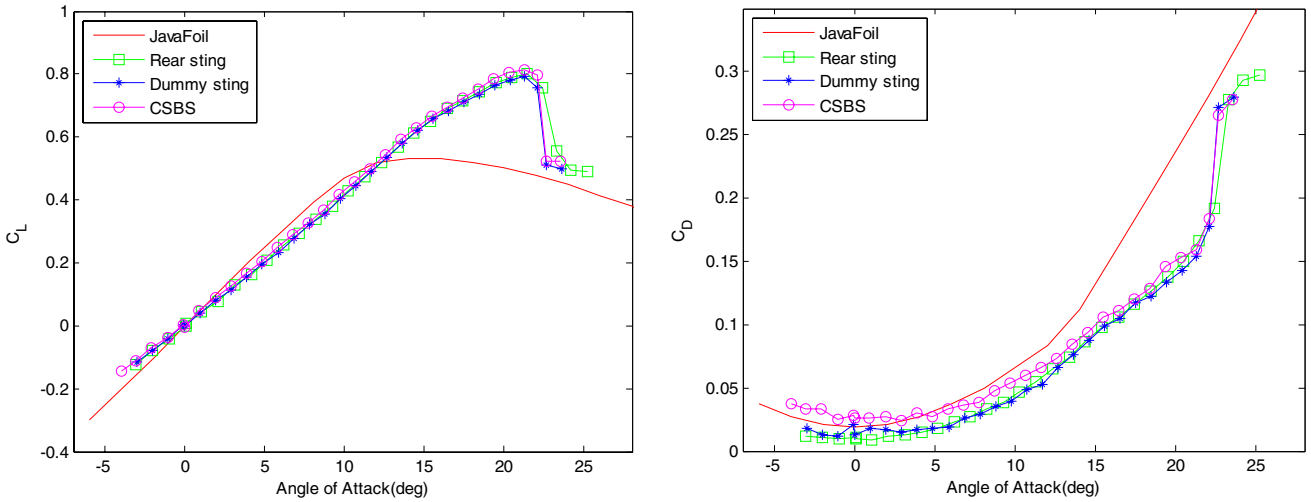

Fig. 16 CL, CD profile at Re = 440,000

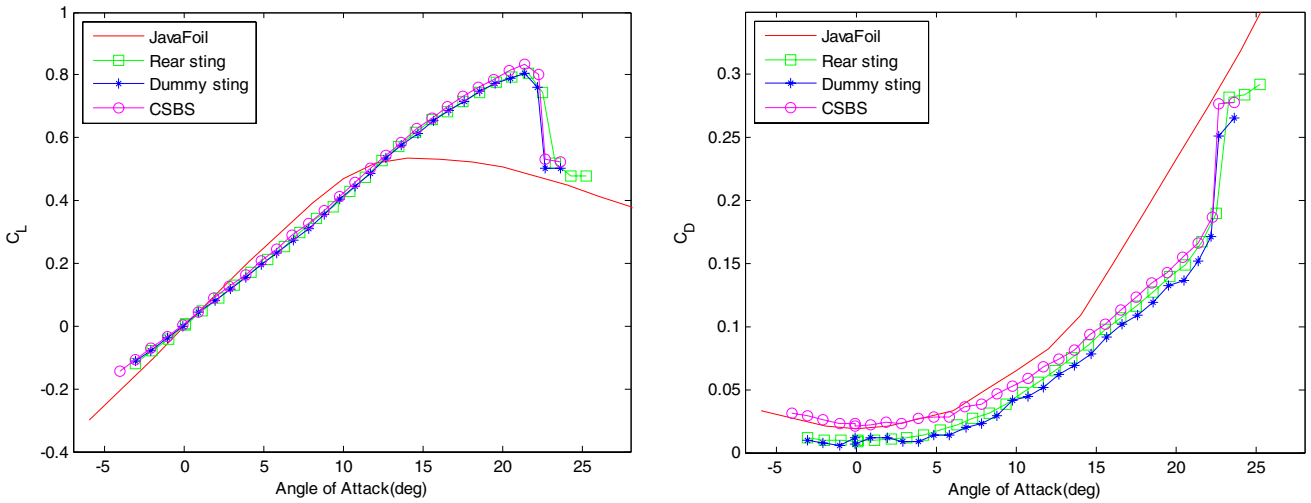

Fig. 17 CL, CD profile at Re = 500,000

that the CSBS acted as a competitive model support against the rear sting support.

In the C_D plots shown in Figs. 16 and 17, some significant deviations can be observed among the three configurations. The C_D values from the rear sting and dummy sting configurations appear to be smaller than those of the CSBS. It was found that the zero-lift and drag of the model are most affected due to sting support interference, and the corresponding drag values decrease. This apparent decrease in the drag is in fact a strong function of the Mach number at subsonic speeds for a certain type of sting geometry [11]. The rear sting can delay the separation of the trailing edge, possibly resulting in less drag [33]. For our modified NACA0015 airfoil, the same aerodynamic phenomena appeared in the C_D plot. However, these differences were diminished at the higher Reynolds number of 550,000, as shown in Fig. 18.

In all of the C_D plots for each Reynolds number, the difference in the C_D profile appears to be very small between the rear sting and dummy sting configurations. The only difference is the existence of the cable support between the two configurations. This indicates that the cable support interference is apparently small compared to that of the rear sting support. All of the comparative test results demonstrate physically meaningful and reasonable characteristics of the support interference.

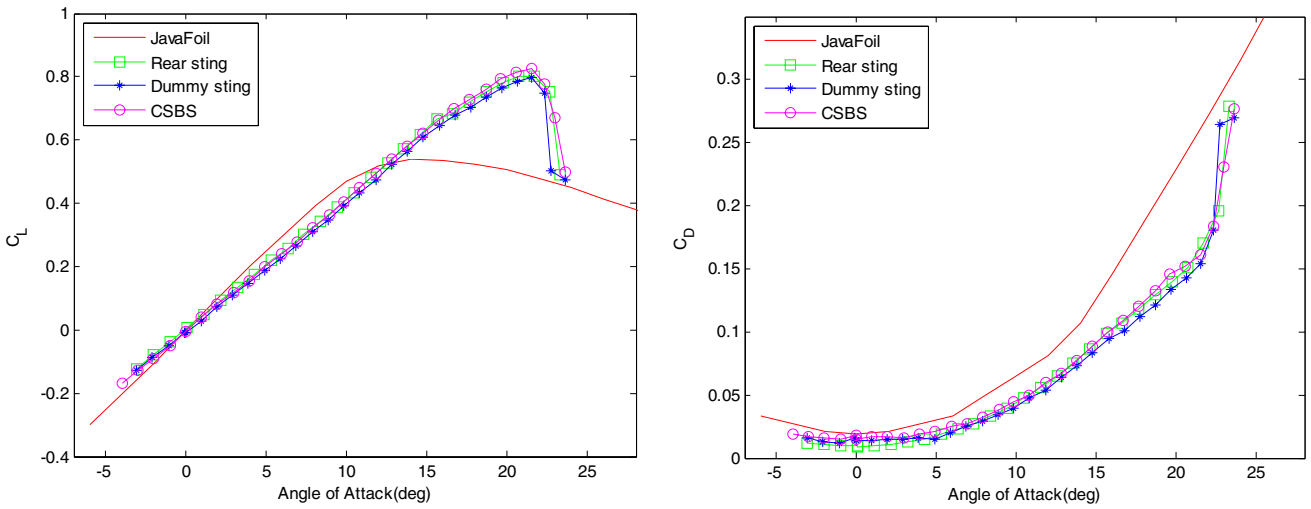

Fig. 18 CL, CD profile at Re = 550,000

4.3 Model Support Vibration

The vibration attenuation characteristics of the cable support were experimentally demonstrated through comparative wind tunnel tests between the rear sting support and the cable support of the CSBS. In these tests, the same modified NACA0015 airfoil model and support systems used in the support interference tests are applied again. Rolling fluctuations of the test model were measured by the motion tracking system to investigate the vibration magnitude as affected by the aerodynamic interference of two model supports. The AOA of the test model was increased to a stall region.

Figure 19 shows the vibration responses from these two support configurations at a Reynolds number of 440,000. The cable support of the CSBS shows much better vibration attenuation characteristics than the rear sting support. The same pattern of tests was repeated while increasing the Reynolds number, as shown in Figs. 20 and 21. In all repeated tests, the cable support showed better vibration attenuation characteristics.

In the introduction, the CSBS was suggested as an alternative device that makes up for the shortcomings of conventional model support methods, such as a sting. From Figs. 19, 20, 21, it is clearly observed that the CSBS is appropriately operated at all angles of attack (AOA) while reducing the vibration of the test model. This implies that the CSBS possesses excellent vibration attenuation characteristics compared to a rear sting model support.

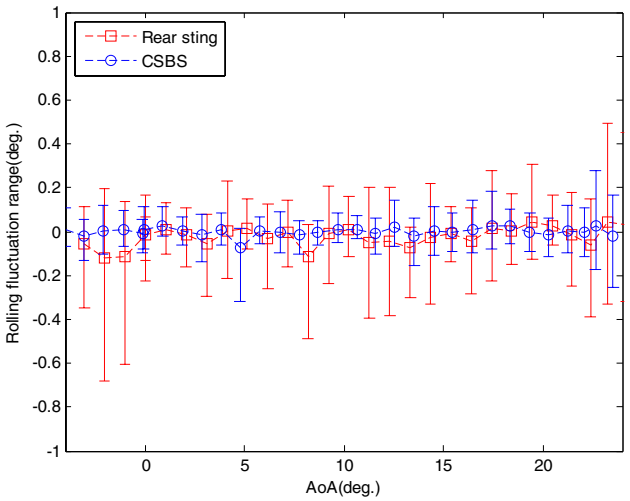

Fig. 19 Rolling fluctuation range at Re = 440,000

5 Conclusion

A cable-driven model support concept is introduced and detailed from the relevant formulation to the implementation of the hardware and software for the CSBS. The developed CSBS is capable of precisely controlling the motion of a test model within ± 250 mm for translation and within ± 30° for rotation. The CSBS was designed to act as a balance measuring aerodynamic load and a motion control device in wind tunnel tests. In the CSBS, load measurements are accomplished using a cable balance consisting of eight load cells connected with pre-tensioned cables. Loading tests and statistical analyses confirmed that the CSBS could accurately measure an aerodynamic load. The effectiveness of the application of the CSBS against aerodynamic interference and vibration was experimentally demonstrated through comparative wind tunnel tests with a rear sting model support. The test results showed that the CSBS acted as a competitive model support against the rear sting support. The aerodynamic interference of the cable support is

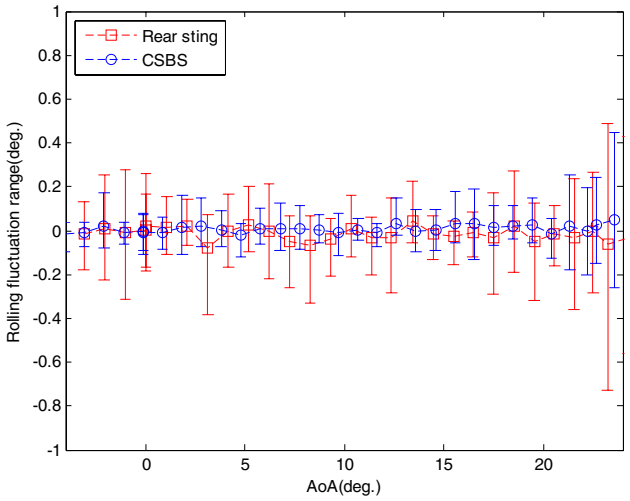

Fig. 20 Rolling fluctuation range at Re = 500,000

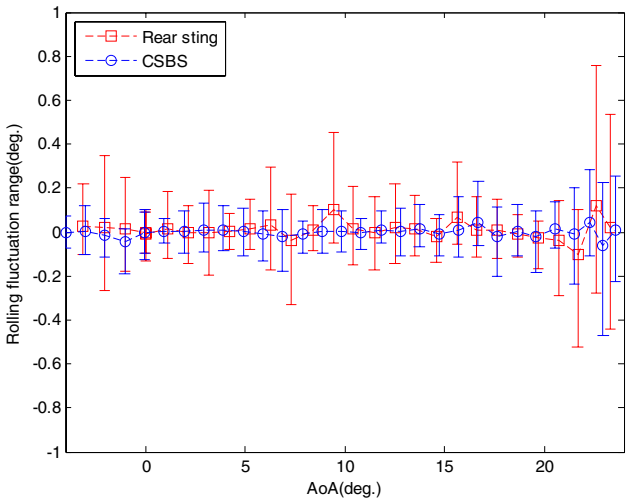

Fig. 21 Rolling fluctuation range at Re = 550,000

insignificant compared to that of the rear sting support and the CSS. Also, the CSBS showed excellent vibration attenuation characteristics at all AOA values, including the stall range in which the conventional cantilever sting frequently cannot reach due to severe vibration. These vibration suppression characteristics allow us easily to expand the test envelope of a wind tunnel.

Open Access This article is licensed under a Creative Commons Attribution 4.0 International License, which permits use, sharing, adaptation, distribution and reproduction in any medium or format, as long as you give appropriate credit to the original author(s) and the source, provide a link to the Creative Commons licence, and indicate if changes were made. The images or other third party material in this article are included in the article's Creative Commons licence, unless indicated otherwise in a credit line to the material. If material is not included in the article's Creative Commons licence and your intended use is not permitted by statutory regulation or exceeds the permitted use, you will need to obtain permission directly from the copyright holder. To view a copy of this licence, visit http://creativecommons.org/licenses/by/4.0/.

References

1. Lee S-H, Han Y-O (2020) Experimental investigation of high-angle-of-attack aerodynamics of low-aspect-ratio rectangular wings configured with NACA0012 airfoil section. Int J Aeronaut Space Sci 21:303–314. https://doi.org/10.1007/s42405-019-00215-z
2. Kim H-H, Kim H-Y, Han J-S, Han J-H (2018) A development and assessment of variable-incidence angle vortex generator at low Reynolds number of ~ 5×10^4. Int J Aeronaut Space Sci 19:836–842. https://doi.org/10.1007/s42405-018-0099-y
3. Erickson GE (1980) Water tunnel flow visualization: insight into complex three-dimensional flowfields. J Aircraft 17(9):656–662. https://doi.org/10.2514/3.57952
4. Han J-S, Kim J-K, Chang J-W, Han J-H (2015) An improved quasi-steady aerodynamic model for insect wings that considers movement of the center of pressure. Bioinspir Biomim 10(4):046014. https://doi.org/10.1088/1748-3190/10/4/046014
5. Suarez CJ, Malcolm GN (1994) Water tunnel force and moment measurements on an F/A-18. In: AIAA 12th Applied Aerodynamics Conference, Colorado Springs, CO, USA. https://doi.org/10.2514/6.1994-1802
6. Yun J-M, Han J-H (2020) Development of ground vibration test based flutter emulation technique. Aeronaut J 124(1279):1436–1461. https://doi.org/10.1017/aer.2020.36
7. Pope A (1947) Wind tunnel testing. Experimental Aerodynamics Division Sandia Corporation, Wiley, London
8. Carter EC (1972) Interference effects of model support systems. Aircraft Research Association Limited Manton Lane, Bedford
9. Rašuo B (2011) The influence of Reynolds and Mach numbers on two-dimensional wind-tunnel testing: an experience. Aeronaut J 115(1166):249–254. https://doi.org/10.1017/S0001924000005704
10. Chang B-H (2000) Numerical evaluation of the strut interference and the 3-run image method for wind tunnel tests. Int J Aeronaut Space Sci 1(2):17–21
11. Ocokoljić G, Rašuo B, Kozić M (2017) Supporting system interference on aerodynamic characteristics of an aircraft model in a low-speed wind tunnel. Aerosp Sci Technol 64:133–146. https://doi.org/10.1016/j.ast.2017.01.021
12. Balakrishna S, Houlden H, Butler DH, White R (2007) Development of a wind tunnel active vibration reduction system. In: 45th AIAA Aerospace Sciences Meeting and Exhibit, Reno, Nevada, USA. https://doi.org/10.2514/6.2007-961
13. Rivers MB, Balakrishna S (2014) NASA common research model test envelope extension with active sting damping at NTF. In: 32nd AIAA Applied Aerodynamics Conference, Atlanta, GA, USA. https://doi.org/10.2514/6.2014-3135
14. Balakrishna S, Butler DH, White R, Kilgore WA (2008) Active damping of sting vibrations in transonic wind tunnel testing. In: 46th AIAA Aerospace Sciences Meeting and Exhibit, Reno, Nevada, USA. https://doi.org/10.2514/6.2008-840
15. Chung J-D, Sung B-Z, Cho T-H (2000) Wind tunnel test of a MRP model using external balance. Int J Aeronaut Space Sci 1(2):68–74
16. Allan MR, Badcock KJ, Barakos GN, Richards BE (2004) Wind-tunnel interference effects on a 70° delta wing. Aeronaut J

108(1088):505–513. https://doi.org/10.1017/S0001924000000336
17. Sung Y-H, Kim H-Y, Han J-H, Lee D-K (2020) Self-learning MAV under safety-guaranteed flight test environment. In: AIAA SciTech Forum, Orlando, FL, USA. https://doi.org/10.2514/6.2020-0261
18. Sung Y-H, Lee D-K, Han J-S, Kim H-Y, Han J-H (2017) MSBS-SPR integrated system allowing wider controllable range for effective wind tunnel test. Int J Aeronaut Space Sci 18(3):414–424. https://doi.org/10.5139/IJASS.2017.18.3.414
19. Rognant M, Courteille E (2018) Improvement of cable tension observability through a new cable driving unit design. In: Gosselin C, Cardou P, Bruckmann T, Pott A (eds) Cable-driven parallel robots, mechanisms and machine science 53, pp 280–291. https://doi.org/10.1007/978-3-319-61431-1_24
20. Farcy D, Llibre M, Carton P, Lambert C (2007) SACSO: wire-driven parallel set-up for dynamic tests in wind tunnel-review of principles and advantages for identification of aerodynamic models for flight mechanics. In: 8th ONERA-DLR Aerospace Symposium, Gottingen
21. Wang X, Hu Y, Lin Q (2017) Workspace analysis and verification of cable-driven parallel mechanism for wind tunnel test. J Aerosp Eng 231(6):1012–1021. https://doi.org/10.1177/0954410016646601
22. Yangwen X, Qi L, Yaqing Z, Bin L (2010) Model aerodynamic tests with a wire-driven parallel suspension system in low-speed wind tunnel. Chin J Aeronaut 23(4):393–400. https://doi.org/10.1016/S1000-9361(09)60233-8
23. Lambert TJ, Vukasinovic B, Glezer A (2016) A six degrees of freedom dynamic wire-driven traverse. Aerospace 3(2):11. https://doi.org/10.3390/aerospace3020011
24. Lambert TJ, Vukasinovic B, Glezer A (2014) Aerodynamic flow control of a moving axisymmetric bluff body. In: 52nd AIAA Aerospace Sciences Meeting, National Harbor, Maryland, USA. https://doi.org/10.2514/6.2014-0932
25. Lambert TJ, Vukasinovic B, Glezer A (2015) Unsteady aerodynamic loads effected by flow control on a moving axisymmetric bluff body. In: 53rd AIAA Aerospace Sciences Meeting, Kissimmee, Florida, USA. https://doi.org/10.2514/6.2015-0827
26. Lambert TJ, Vukasinovic B, Glezer A (2016) Aerodynamic control of coupled body-wake interactions. In: 54th AIAA Aerospace Sciences Meeting, San Diego, California, USA. https://doi.org/10.2514/6.2016-0053
27. Lambert TJ, Vukasinovic B, Glezer A (2018) Aerodynamic flow control of axisymmetric bluff body by coupled wake interactions. AIAA J 56(8):2992–3007. https://doi.org/10.2514/1.J056782
28. RTRI. Moving belt, wire balance. http://www.rtri.or.jp/rd/maibara-wt
29. Gagliardini L, Caro S, Gouttefarde M, Girin A (2016) Discrete reconfiguration planning for cable-driven parallel robots. Mech Mach Theory 100:313–337. https://doi.org/10.1016/j.mechmachtheory.2016.02.014
30. Niku SB (2001) Introduction to robotics: analysis, systems, applications. Prentice Hall
31. Roberts RG, Graham T, Lippitt T (1998) On the inverse kinematics, statics, and fault tolerance of cable-suspended robots. J Robot Syst 15(10):581–597. https://doi.org/10.1002/(SICI)1097-4563(199810)15:10%3c581::AID-ROB4%3e3.0.CO;2-P
32. Park K-Y, Sung Y-H, Han J-H (2020) Development of a cable suspension and balance system and its novel calibration methods for effective wind tunnel tests. Measurement 2020:108717. https://doi.org/10.1016/j.measurement.2020.108717
33. Kawamura Y, Takenaga T, Oh J-B, Takahashi T, Kwon C-K, Mizota T (2004) Development of a low electric power 40 cm class magnetic suspension and balance system. J Wind Eng 29(1):117–127. https://doi.org/10.5359/jwe.29.98_117

Publisher's Note Springer Nature remains neutral with regard to jurisdictional claims in published maps and institutional affiliations.